

International Journal of Masonry Research and Innovation

ISSN online: 2056-9467 - ISSN print: 2056-9459

<https://www.inderscience.com/ijmri>

Experimental, analytical, and numerical investigations on bond behaviour of basalt TRM systems

Eloisa Fazzi, Giulia Misseri, Luisa Rovero

DOI: [10.1504/IJMRI.2022.10051005](https://doi.org/10.1504/IJMRI.2022.10051005)

Article History:

Received:	30 August 2021
Accepted:	09 February 2022
Published online:	14 March 2023

Experimental, analytical, and numerical investigations on bond behaviour of basalt TRM systems

Eloisa Fazzi, Giulia Misseri* and Luisa Rovero

Dipartimento di Architettura,
Università di Firenze,
Piazza Brunelleschi 6, 50121, Firenze, Italy
Email: eloisa.fazzi@unifi.it
Email: giulia.misseri@unifi.it
Email: luisa.rovero@unifi.it
*Corresponding author

Abstract: In this study, a composite system designed for the reinforcement of masonry structures is investigated. The constituents of the composite system are a basalt-fibre mesh and a lime-based mortar matrix. Two basalt-fibre mesh textiles showing one double the reinforcement of the other due to a tighter spacing of yarns were considered. Three solutions were tested: one layer of the looser textile, one layer of the tighter, and two layers of the looser one, which provided the same reinforcement ratio of the tighter. The experimental campaign addressed single-lap shear tests on bricks. Also, within a fracture process zone approach, bond behaviour of the composite system, is modelled in closed form assuming a trilinear cohesive material law, CML, and solving the system of differential equations. Further, a numerical finite-difference model, based on the same trilinear CML of the analytical model, is set up and compared to experimental results.

Keywords: basalt fibres; lime mortar; FRCM; TRM; cohesive material law; CML; finite-difference; single-lap shear test; bond test; direct shear test.

Reference to this paper should be made as follows: Fazzi, E., Misseri, G. and Rovero, L. (2023) 'Experimental, analytical, and numerical investigations on bond behaviour of basalt TRM systems', *Int. J. Masonry Research and Innovation*, Vol. 8, Nos. 2/3, pp.333–354.

Biographical notes: Eloisa Fazzi is a PhD student in Structures and Restoration of Architecture and the Cultural Heritage at the Department of Architecture of the University of Florence. She received her Bachelors in Philosophy at the Catholic University of Milan, then Bachelors and Masters in Architecture at the University of Florence. Her thesis investigates the bond behaviour of fibre-reinforced cementitious matrices, both through experimental campaigns and the implementation of numerical models.

Giulia Misseri received her PhD in Structures and Restoration of Architecture and the Cultural Heritage from the University of Florence in 2017. She is currently an Assistant Professor at the University of Florence. Her research interests include statics and dynamics of masonry structures, fracture mechanics and experimental testing.

Luisa Rovero is an Associate Professor of Structural Mechanics at the Department of Architecture, University of Florence. She is a member of the Committee of the PhD Curriculum Structures and Restoration of Architecture and the Cultural Heritage of PhD in Architecture of the University of Florence. Her current research activity is mainly focused on the mechanical behaviour of masonry structures, analysis and modelling of fibre-reinforced inorganic matrix materials for the reinforcement of masonry structures.

This paper is a revised and expanded version of a paper entitled 'Experimental, analytical, and numerical investigation on bond behaviour of basalt TRM systems' presented at ICSCES – The International Conference of Steel and Composite for Engineering Structures, Ancona, Italy, 12–13 July 2021.

1 Introduction

Based upon the results of recent studies and applications, fibre reinforced composite materials appear a promising option due to their structural efficiency (strength to mass ratio) and ease of application. The inherent vulnerability of unreinforced masonry structures belonging to the cultural heritage calls for suitable strengthening techniques, which allow for compatibility and reversibility of interventions. Fibre reinforced composite strengthening is primarily a component-level strengthening technique (reinforcement of wall panels, arches and vaults and confinement of columns, for example). System-level strengthening techniques can guarantee adequate safety if a component-level connection (wall-to-wall and roof/floor-to-wall) check is performed. First developed as fibre reinforced polymers (FRP) in other branches of applied technologies, lately, they have been introduced in the construction field (Kouris and Triantafillou, 2018; Gattesco and Boem, 2019). To overcome some significant drawbacks caused by the organic binder of FRP matrices – namely low resistance to high temperature, low vapour permeability and failure by delamination from the substrate, fibre reinforced cementitious mortars (FRCM) have been developed using loose mesh textiles and cement or lime-based mortars (Briccoli Bati et al., 2007; Rovero et al., 2013; Rotunno et al., 2015; Alecci et al., 2016; Misseri et al., 2019a, 2019b; Kumar et al., 2019; Barducci et al., 2020; Misseri et al., 2020; Padalu et al., 2020; Boem and Gattesco, 2021), which ensure better compatibility with the masonry substrate. Gypsum based mortars proved also effective (Rovero et al., 2020; Misseri et al., 2021).

Experimental evidence shows that failure of FRCM applied to masonry is driven by the weaker interface, which is the matrix-fibre interface, nonetheless, substrate-composite debonding have been recorded when some flaws in the specimen fabrication process occur. The geometrical configurations of yarn and the textile influence the stress transfer mechanism that is activated both at the fibre-mortar interface and between filaments of the yarn. The mesh looseness determines the contact surface between mortar layers, i.e., in tighter meshes the matrix is somehow prevented from flowing through the textile openings. Indeed, the penetration of the matrix between yarn filaments is closely dependent on the mortar grain size, causing differential strain states and finally, telescopic failure (Kouris and Triantafillou, 2018).

Although a set of standard testing procedures is acknowledged by institutions (ACI Committee 549, 2013; RILEM TC 250-CSM, 2018), the presence of shortcomings

emerges in the literature. In De Santis et al. (2018) the authors conclude that tensile tests on composite coupons, single-lap shear tests and tensile tests on free fabric cannot be considered alternatively. Furthermore, in Dalalbashi et al. (2018a, 2018b) the comparison between the cohesive material laws (CMLs) obtained by pull-out and shear bond tests suggests that transversal yarns constituting the textile play a crucial role and shear bond tests provide a closer representation of the actual response mechanism of a FRCM. Moreover, results are influenced by many other factors, such as FRCM-masonry interface, mortar cracking rates, boundary effects etc., and must be interpreted carefully. In Ceroni and Salzano (2018), an extensive review of experimental campaigns on bond test supports the idea of a relation between mechanical properties of the substrate and the strains attained by the FRCM jacket.

In this framework, basalt-based textiles represent one of the latest alternatives among fibre reinforcements. Although being a valid competitor of other systems (e.g., glass fibre based), still, some issues are connected to durability in alkali environments. Hence, design and testing guidelines developed for other systems shall consider such peculiar characteristics carefully (Monaldo et al., 2019). A series of round-robin tests is carried out in Lignola et al. (2017) on various basalt-based systems by different research units, performing tests on bare fibres, on composite coupons and bond tests. Reported values of the fibre-mortar relative displacement highlight a significant scatter not only among different composite systems, but also between different testing apparatus for the same composite. Tensile tests on basalt composite coupons carried out in (Caggegi et al., 2017) show that multiple textile layers lead to premature slippage decreasing bonding between fibre and matrix. Moreover, maximum stress in the fibre is recorded for lower reinforcement ratio.

The fibre-matrix interface is often modelled through a Mode-II fracture CML, the fracture energy of which balances the strain energy in the fibre. Once the CML is assumed, it is possible to investigate the behaviour of the bond, determining the trend of interface slip, interface tangential stress, strain in the fibre and finally the fibre tensile force. The parameters of CML can be determined indirectly through back calibration from the global load-slip relationship obtained from experimental bond tests, and different shapes might be better suited for specific systems (Rovero et al., 2020; Misseri et al., 2021).

Modelling fibre-matrix bond behaviour of FRCM is considered in some recent studies. The analytical model presented in Grande et al. (2018), and derived from FRP modelling (Yuan et al., 2004), provides a 1D schematisation accounting for upper and lower fibre-to-matrix interfaces with a bilinear CML; the study focuses on the transition between debonding and slip failure of the composite through different damage scenarios. Effects of grid configuration, which can deeply influence the damage pattern, cannot however be included. Concerning Finite Element simulations of single-lap shear tests, in Grande and Milani (2018), a 2D nonlinear spring model is employed to simulate both interfaces, composite constituents and adherend of single-lap shear tests; the FE model is benchmarked with commercial code. In Donnini et al. (2018) an in-house 2D FEM model based on incremental energy minimisation, including internal damage variable and friction at the fibre matrix-interface, is employed to tackle the differences in single lap shear tests with different fibre pre-coatings. Razavizadeh et al. (2014) propose a wide parametric investigation of 2D plane-stress models through a commercial code, considering plate elements for adherend and mortar, linear truss elements for fibre textile and edged-to-edge nonlinear interfaces to represent fibre-matrix interaction. Carozzi

et al. (2014) use two FEM approaches to model bond tests. The first approach envisages a simplified 2D trussed structure, representing the fibre textile, and makes use of 1D nonlinear interfaces placed at textile joints to account for fibre – mortar interaction. The second FE modelling approach considers a complete 3D model with rigid brick elements interconnected by nonlinear interfaces for substrate and mortar, and a 2D nonlinear trussed structure connected to mortar element through interfaces for fibre textile.

In Soranakom and Mobasher (2010a, 2010b), a finite difference method model is proposed to interpret tensile tests on different FRCM systems. In Fazzi et al. (2022), the authors present an advancement of the finite difference model of Soranakom and Mobasher (2010a) concerning the condition of load application in the uncracked state of the specimen under uniaxial tensile test; the model is employed here to represent single direct shear tests accounting also for the limited tensile strength of the textile. In Nerilli et al. (2020) a micro-scale finite element model is employed to reproduce the typical behaviour of a representative unit area constituted by a textile mesh cell and the surrounding matrix in clamping tensile tests. In Bilotta and Lignola (2021), a finite difference model is applied to simulate bond tests on typical PBO-FRCM and Glass-FRCM including delayed stiffness activation for the fibre textile but neglecting its possible tensile failure. Further research and experimental investigation are still needed to improve soundness and accessibility of analytical and numerical models, considering the variability of composite systems and the many factors that influence the mechanical response.

In this study, an experimental campaign is carried out performing single-lap shear tests on three basalt-based composite typologies. The specimen mesh looseness and the number of textile layers are varied, while the lime-based mortar is kept identical. On the basis of experimental results of bond tests, the parameters of a trilinear CML are indirectly determined through analytical back calibration from the experimental global load-slip diagram. The obtained CML is therefore employed in a finite difference numerical model developed to simulate the mechanical behaviour recorded during the bond tests carried out experimentally. The global load-slip diagram, obtained with the analytical model and derived from the CML calibration, is compared with the diagrams obtained with the finite difference numerical model. The comparison provides good agreement and, hence benchmarking the applied numerical model. A sensitivity analysis of the finite difference model addressing the reinforcement ratio and the related bonding surface is reported afterwards. The finite difference model proposed is easy to implement, and can address, differently from the analytical one, the limited tensile capacity of fibres and the displacement-controlled test typology, soundly tackling the post-peak equilibrium path. The finite difference model therefore constitutes a convenient analysis tool, applied here to carry out an in-depth study on the influence of reinforcement ratios on the response in bond tests for the basalt composite system analysed.

2 Materials and methods

2.1 Tests and specimens

Along with the characterisation of the composite constituents, three composite types were considered in the experimental campaign. The three types had the same matrix, but two textile geometries arranged differently and based on basalt fibres. The wider textile

showed 17 mm-spaced yarns (and equivalent thickness $t_f^* = 0.032$ mm) and the tighter one showed 8 mm-spaced yarns (equivalent thickness $t_f^* = 0.064$ mm); hence, providing double the reinforcement ratio. Composite type 1 was fabricated with a single layer of the wider textile. Composite type 2 was assembled with a single layer of the tighter textile and composite type 3 was implemented with two layers of the wider textile. In so doing, the reinforcement ratio of the composite type 3 was equal to the composite type 2 (the one with the tighter mesh) and double the composite type 1. Hence, the reinforcement ratio increase was obtained in two ways:

- 1 by reducing the spacing of yarns
- 2 by doubling the number of textile layers.

Both the tighter and the wider textiles were constituted by basalt yarns and steel AISI 350 micro-filaments, the mesh was balanced, bi-directional, and coated with alkali-resistant treatment. Joints between the weft and warp yarns appeared woven and thermally sealed. The mechanical characterisation of the basalt-based composite was carried out through an experimental campaign comprising two stages: tests on the constituent materials; bond tests on the composite applied to a brick substrate. The list of tests and the number of tested specimens in brackets are:

- three-point bending (5) and compression tests (10) on the mortar (EN-1015-11, 2019)
- uniaxial tensile tests on the tighter textile made of 1(3), 3(3) and 7 (3) yarns
- uniaxial tensile tests on the wider textile made of 1(3), 2(3), 3(3) and 4(2) yarns
- single-lap shear test (6) on brick with the wider textile (composite type 1)
- single-lap shear test (6) on brick with the tighter textile (composite type 2)
- single-lap shear test (4) on brick with two layers of the wider textile (composite type 3).

2.2 Tests of composite constituents

Stress-strain diagrams recorded during uniaxial tensile tests on single yarns and textile mesh are shown in Figure 3 to Figure 4, and Table 1 reports detailed values of the main mechanical parameters obtained. For all the 20 specimens, with a varying number of yarns, tests provided a mean tensile strength $f_{tf} = 828$ MPa (CV = 0.167) and Young's modulus $E_{tf} = 54.9$ GPa (CV = 0.093). As expected, the sample with seven yarns showed more marked delayed stiffness activation, caused by the relative slip among filaments of the same yarn (Figure 3), hence, a lower value of Young's modulus was recorded. For single and triple filament samples delayed stiffness activation was less noticeable.

Concerning tests on mortar, results reported in Figure 1 to Figure 2 show a mean flexural strength $f_{bm} = 3.01$ MPa (CV 0.115, 5 specimens) and mean compressive strength $f_{cm} = 8.48$ MPa (CV 0.077, 10 specimens).

Figure 1 Results of three-point bending tests on the mortar matrix (see online version for colours)

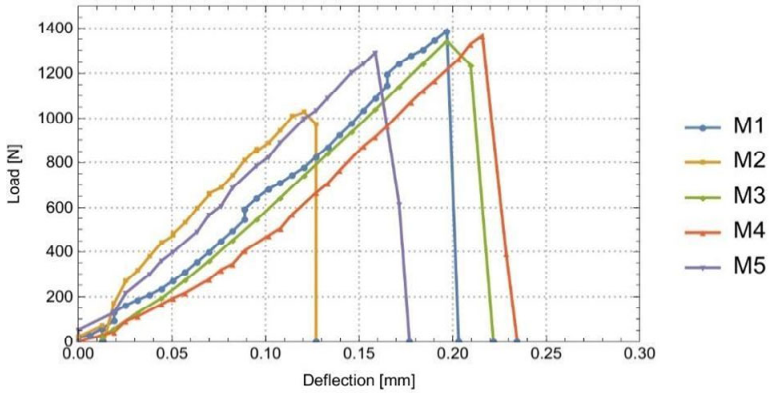


Figure 2 Results of uniaxial compression tests on the mortar matrix (see online version for colours)

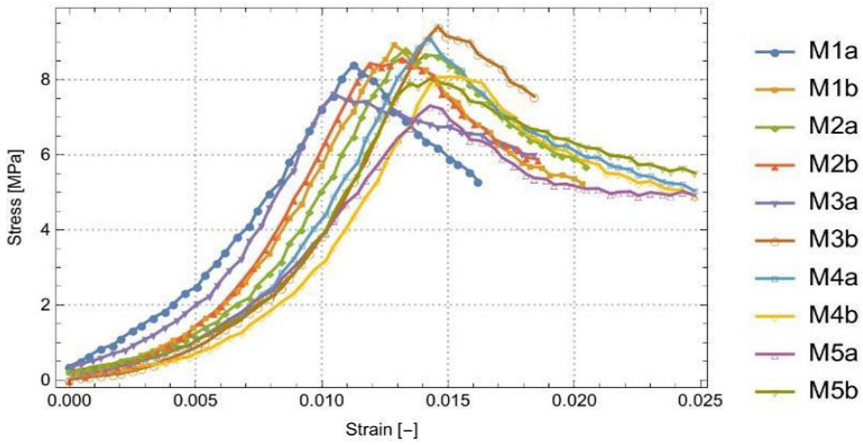


Figure 3 Results of uniaxial tension tests on the tight basalt textile considering, (a) one (b) three (c) seven yarns (see online version for colours)

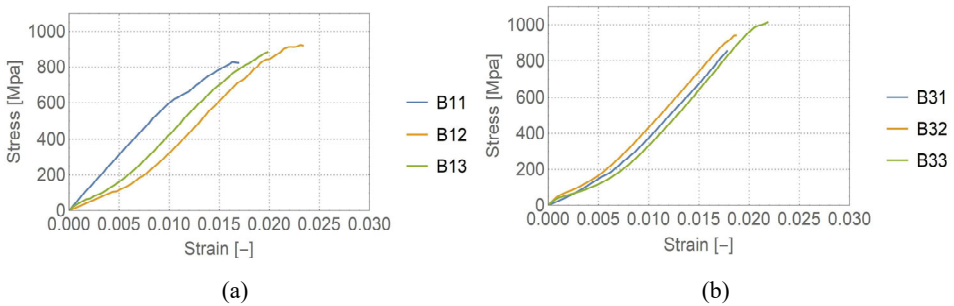
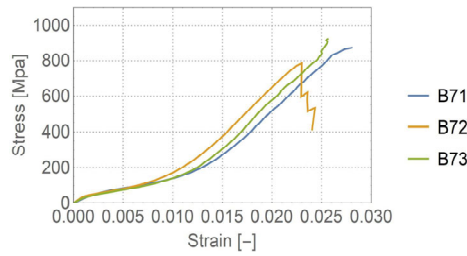


Figure 3 Results of uniaxial tension tests on the tight basalt textile considering, (a) one (b) three (c) seven yarns (continued) (see online version for colours)



(c)

Figure 4 Results of uniaxial tension tests on the loose basalt textile for, (a) one (b) two (c) three (d) four yarns (see online version for colours)

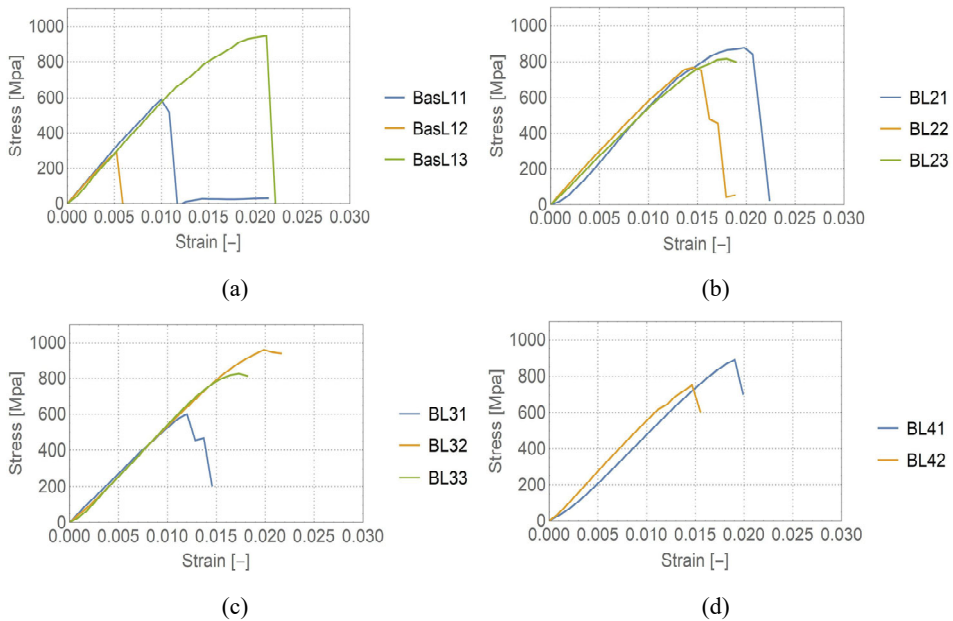


Table 1 Results of tension tests on tight fibre mesh (left) and loose mesh (right)

spec	f_{if}	E_{if}	ϵ_{if}	spec	f_{if}	E_{if}	ϵ_{if}
	[MPa]	[MPa]	[-]		[MPa]	[MPa]	[-]
B11	833	61,755	0.017	BL11	590.64	62,078	0.010
B12	928	57,874	0.025	BL12	300.82	58,848	0.005
B13	884.97	56,685	0.021	BL13	949.41	57,449	0.021
B31	861.44	58,415	0.02	BL21	881.34	54,798	0.020
B32	947.06	56,136	0.022	BL22	774.31	59,659	0.015
B33	1,021.5	58,492	0.026	BL23	819.53	54,616	0.018

Note: Symbols refer to f_{if} fibre tensile strength, fibre tensile Young's modulus E_{if} and fibre strain at rupture ϵ_{if} .

Table 1 Results of tension tests on tight fibre mesh (left) and loose mesh (right) (continued)

<i>spec</i>	f_{if}	E_{if}	ε_{uf}	<i>spec</i>	f_{if}	E_{if}	ε_{uf}
	[MPa]	[MPa]	[-]		[MPa]	[MPa]	[-]
B71	876.73	46,267	0.029	BL31	601.50	54,741	0.012
B72	786.95	45,877	0.025	BL32	960.53	53,175	0.020
B73	923.63	46,942	0.031	BL33	829.28	54,144	0.017
				BL41	891.06	46,546	0.019
				BL42	761.28	55,843	0.015
<i>Av.</i>	895.92	54,272	0.024	<i>Av.</i>	759.97	55,627	0.016
<i>CV.</i>	0.077	0.113	0.185	<i>CV.</i>	0.257	0.073	0.306

Note: Symbols refer to f_{if} fibre tensile strength, fibre tensile Young's modulus E_{if} and fibre strain at rupture ε_{uf} .

2.3 Single-lap shear tests

For composite types 1 and 3, direct single-lap shear tests specimens were prepared, after duly moistening bricks, by casting in a specific mould a 5 mm thick mortar layer. Afterwards, a textile reinforcement 750 mm long, and 95 mm width, was positioned with slight pressure to enhance fibre impregnation. Then a second 5 mm mortar layer was laid, reaching a total thickness of 10 mm of the jacket. For composite type 2, after the first 5 mm layer of mortar and the textile were placed, another layer of mortar was applied with 3 mm thickness. Then the second textile was placed, and the mortar was cast up to 10 mm total thickness. According to mesh looseness, 6 longitudinal yarns were embedded in composite type 1 and 3, and 11 longitudinal yarns in composite type 2. All specimens were cured in a controlled environment, i.e., 20°C and 50% relative humidity, for 28 days. The non-embedded textile reinforcement was wrapped around a steel cylinder and glued to it through a bi-component resin, which was also applied to the entire length of bare textile. Two cantilever displacement transducers were placed at the end of the jacket, one on top of the steel cylinder and another on one side of the brick (Figure 5). Tests were carried out by displacement control using a 50-kN load cell (type TCLP—5B, Tokyo Sokki Kenkyujo Co. Ltd). The control parameter was the slip of the fibre at the end of the mortar jacket. Specimens were labelled SSTN-n, where N indicates the composite type tested and n was the identification number.

Comparing test results in terms of load-slip diagrams, Figure 6, Figure 7 and Figure 8, it can be noted that SST1 and SST3 samples showed an initial linear elastic phase followed by a pre-peak stiffness loss and a steep post-peak descending branch. The quality of diagrams and direct observations on the specimens after tests suggest a gradual failure due to slippage up to rupture of periphery fibre yarns. Differently, the SST2 sample failed for fibre-matrix interface debonding showing, after a very short linear elastic phase, a nearly horizontal branch in the diagram. It is also worth noting that samples SST1 reached peak load values on the average higher than those reached during tests of the samples SST2, although SST1 was characterised by half the amount of the reinforcement. Moreover, sample SST2 reached load values between 4 and 6 times lower than those reached by the SST3, despite having the same reinforcement ratio. The fact that two layers of the wider mesh, i.e., samples SST3, are highly more effective in

providing adequate bonding can be deduced by observing Figure 9, where results of bond tests are reported in terms of stress and slip.

Figure 5 Image of (a) set up used for single-lap shear tests and of (b) an instrumented specimen (see online version for colours)

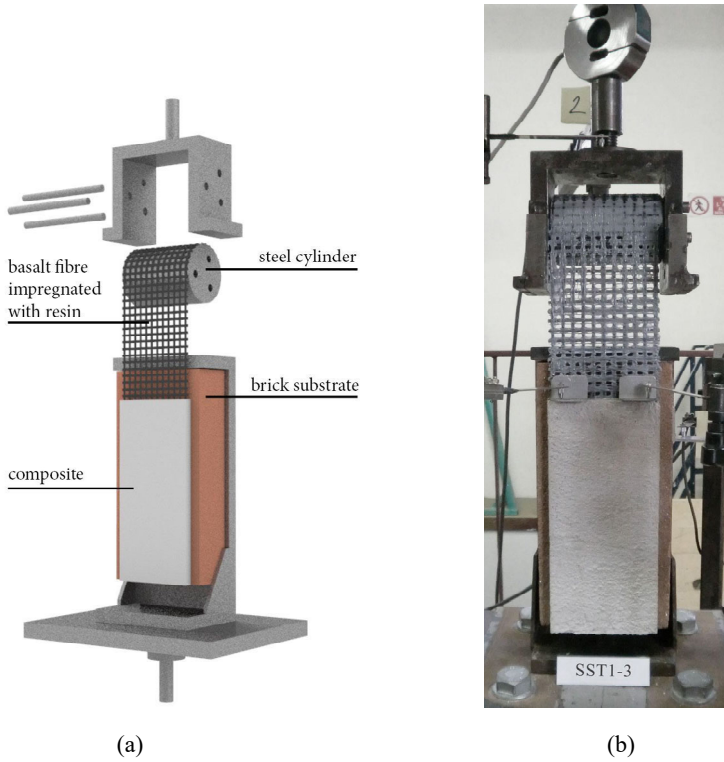


Figure 6 Results of bond tests on specimen type 1: SST1 (see online version for colours)

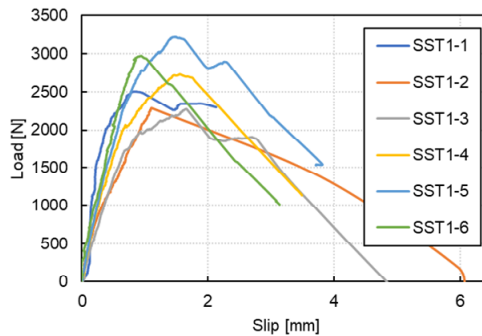


Figure 7 Results of bond tests on specimen type 2: SST2 (see online version for colours)

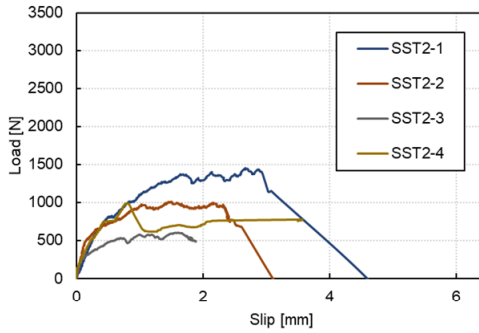


Figure 8 Results of bond tests on specimen type 3: SST3 (see online version for colours)

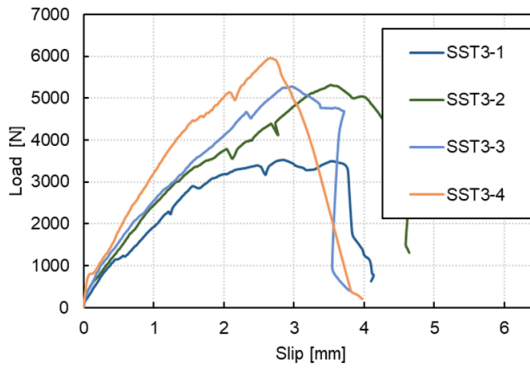
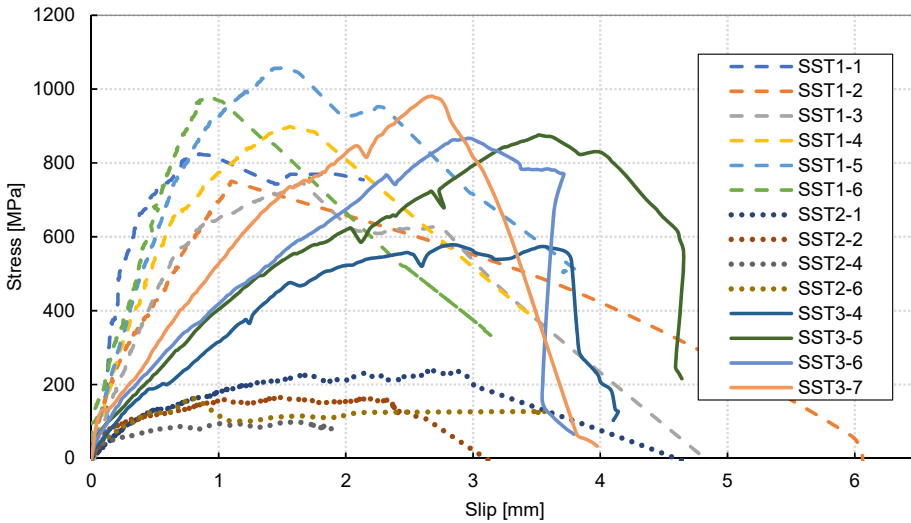


Figure 9 Stress-slip diagrams of bond tests results (see online version for colours)



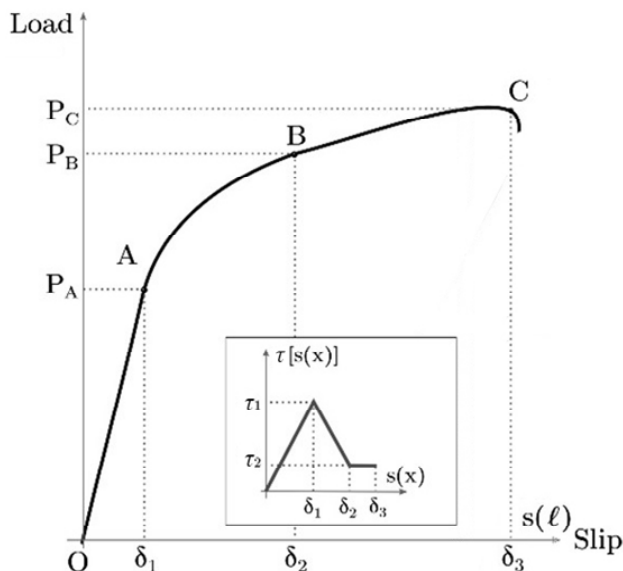
3 Models for the interpretation of experimental results

3.1 Problem statement and closed-form solution

The typical load-slip diagram of a single-lap shear test, Figure 10, shows an initial linear elastic behaviour of the material, identified by a segment with constant slope until point $A(\delta_1; P_1)$. Afterwards, the response of the material becomes nonlinear, but the load value continues to increase up to point $B(\delta_2; P_2)$. A further branch until the peak load is reached at point $C(\delta_3; P_3)$ (see Figure 10).

In the framework of cohesive fracture mechanics, changes in the quality of the response on the global load-slip curve are related to different shear transfer mechanisms at the interfaces. Therefore, the shape of the global load-slip diagram depends on the mechanism activated by the slippage between the fibre and the matrix, which is described by a bond-slip relation, also called CML. Since the shear transfer mechanism takes place at the internal interfaces of the composite, i.e., the matrix-fibre interfaces, adequate observational evidence about it is not yet available and the CML calibration can be tackled through an indirect approach.

Figure 10 Relation between global load slip curve and local CML, where points $A(\delta_1; P_1)$, $B(\delta_2; P_2)$ and $C(\delta_3; P_3)$ correspond to the change in the branches



Through indirect calibration of the CML, and assuming a trilinear shape ending with a frictional plateau, the slippage values registered at points A, B, C identify different shear transfer mechanisms in the CML, being $\delta_1, \delta_2, \delta_3$ respectively the abscissa of the endpoint of the linear elastic, softening, and frictional branch.

$$\tau[s(x)] = \begin{cases} \frac{\tau_1}{\delta_1} s(x); & 0 < s(x) \leq \delta_1 \\ \frac{\tau_1 - \tau_2}{\delta_1 - \delta_2} [s(x) - \delta_1] + \tau_1 & \delta_1 < s(x) \leq \delta_2 \\ \tau_2 & \delta_2 < s(x) \leq \delta_3 \end{cases} \quad (1)$$

The values of τ_1 and τ_2 are obtained equating the work done by the fibres during the elongation and the work done by the shear stress at the interfaces due to fibre slip:

$$A_f E_f \int_0^x \left(\int_0^{\varepsilon_f(x)} \varepsilon_f d\varepsilon_f \right) dx = \psi \int_0^x \left(\int_0^{s(x)} \tau[s(x)] ds \right) dx \quad (2)$$

where A_f is the cross sectional area of the reinforcing fibre, given as b_f width of the textile multiplied for t_f^* equivalent thickness; ε_f is the strain of the fibre, E_f is Young’s modulus of the fibre, $\tau(s) = \tau[s(x)]$ is the CML and ψ is the fibre-matrix bonding perimeter calculated by assuming a circular cross section for each embedded yarn as $\psi = 2\sqrt{mA_f\pi}$ with m number of yarns. For $x = L$, equation (2) provides the relation between the fracture energy and the applied load, P_i , at the generic point of the global load-slip diagram:

$$P_i = \sqrt{2\psi A_f E_f G_i} \quad (3)$$

The mode-II fracture energy per unit area, G_i , corresponds to the area underneath the CML at specific points of the load-slip diagram, hence, for a trilinear CML:

$$\tau_1 = \frac{P_A^2}{\psi A_f E_f \delta_1} \quad (4)$$

$$\tau_2 = \frac{P_B^2}{\psi A_f E_f (\delta_1 - \delta_2)} + \frac{\delta_2 \tau_1}{\delta_1 - \delta_2} \quad (5)$$

where P_A and P_B are the load value at the end of the elastic and elastic-softening phases, respectively.

Equilibrium of the infinitesimal portion of the composite, referred to the simplified model of Figure 11(a), is:

$$[\sigma_f(x) + d\sigma_f(x)] A - [\sigma_f(x)] A_f - \psi \tau[s(x)] dx = 0 \quad (6)$$

where σ_f is the fibre stress; hence:

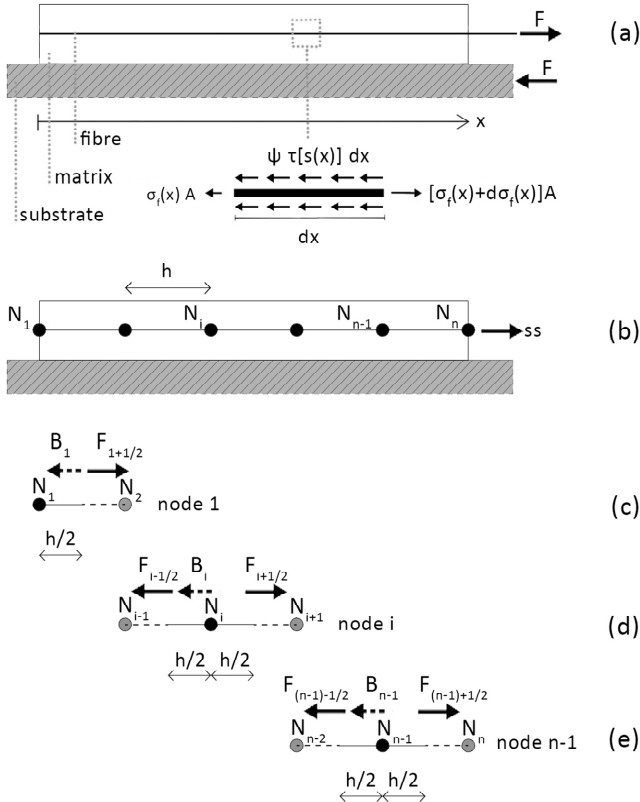
$$\frac{d\varepsilon_f(x)}{dx} E_f A_f = \psi t[s(x)] \quad (7)$$

For the compatibility condition between slips and strains, $\frac{ds(x)}{dx} = \varepsilon_f(x)$, the following differential equation sets the problem.

$$\frac{d^2s(x)}{dx^2} = \frac{\psi}{A_f E_f} \tau[s(x)] \quad (8)$$

Since a trilinear CML is here selected, the general solution of the interface problem provided by the above equation must be specialised for each segment of the global load-slip diagram. The enforcement of appropriate boundary and continuity conditions provides the analytical description of the global load-slip diagram. The calibration of the CML is obtained by selecting the points P_i in the experimental diagram in order to obtain the best fit between the analytical and experimental diagrams.

Figure 11 Schematization of single lap shear test and equilibrium free body diagram of an infinitesimal portion of the embedded fibre (a) scheme of the discretisation of the embedded length of pull-out specimen (b), and free body diagrams of representative nodes of the finite difference model (c), (d), (e)



3.2 Finite-difference model setup

A finite-difference model of shear transfer mechanisms at fibre-matrix interfaces is developed, on the basis of the model proposed in Soranakom and Mobasher (2010a) for coupon tension test and refined in Fazzi et al. (2022) for the condition of load application. Using the CML obtained through the back calibration in the analytical method, the finite-difference model is employed to simulate the experimental tests described in Section 2, and results obtained are also compared with those obtained from the analytical model.

The model is implemented considering the single-lap shear test as a mono-dimensional problem, represented by a longitudinal section of the specimen, where the reinforcing fabric is modelled through a linear elastic straight yarn with limited tensile strength. The embedded length is discretised into $n-1$ segments, delimited by n nodes at constant spacing h . Boundary conditions are enforced as follows: at the free-end (node N_1) the strain of the yarn is imposed equal to 0, while at the loaded end (node N_n) a defined fibre slip ss is prescribed incrementally, to simulate the displacement control testing procedure. Assuming that the axial stiffness of the fibre is remarkably lower than the one of the matrix, matrix strain can be neglected.

According to the finite-difference method, the bond stress is supposed to be constant over half spacing before and half spacing after each node of the discretisation. With reference to the free-body diagrams shown in Figure 11(c), Figure 11(d), and Figure 11(e) equilibrium condition is reported for three typical nodes, which defines the model: N_1 , N_i , and node N_{n-1} , respectively defining conditions at the free-end, along the embedded length, and at the loaded-end.

- *Free end.* At the free end, equilibrium is written at distance $h/2$ from node N_1 , where the acting force $F_{1+1/2}$, generated by the slip of the loaded end, must be balanced by the bond resistance force of the fibre B_1 [Figure 11(c)].

$$F_{1+\frac{1}{2}} - B_1 = 0 \tag{10}$$

where

$$F_{1+\frac{1}{2}} = A_f E_f \frac{(s_2 - s_1)}{h} \tag{11}$$

$$B_1 = \frac{1}{2} \psi k_1 s_1 h \tag{12}$$

In equations (11) and (12), k_i is the secant modulus of the CML at generic node N_i , s_i is the slip at the same generic node, and ψ is the fibre perimeter. Inputting equations (11) and (12) in equation (10) yields

$$-\left[A_f E_f + \frac{1}{2} \psi k_1 h^2 \right] s_1 + A_f E_f s_2 = 0 \tag{13}$$

- *Interior nodes.* For a typical interior node N_i , with $i = 2; \dots; n-2$, the equilibrium is written through the central difference [Figure 11(d)]:

$$F_{i+\frac{1}{2}} - F_{i-\frac{1}{2}} - B_i = 0 \tag{14}$$

Similarly to equation (11) and (12), the acting forces and the bond force become:

$$F_{i+\frac{1}{2}} = A_f E_f \frac{(s_{i+1} - s_i)}{h} \tag{15}$$

$$F_{i-\frac{1}{2}} = A_f E_f \frac{(s_i - s_{i-1})}{h} \tag{16}$$

$$B_1 = \psi k_i s_i h \quad (17)$$

The equilibrium equation is therefore:

$$A_f E_f s_{i-1} - [A_f E_f + \psi k_i h^2] s_i + A_f E_f s_{i+1} = 0 \quad (18)$$

- *Loaded end.* Since at loaded-end slip is imposed incrementally, slip of node N_n is known and no equilibrium equation is needed. Conversely, the known slip ss is to be implemented in the equilibrium equation of node N_{n-1} [Figure 11(e)], where generic nodes N_{i-1} and N_{i+1} of equation (18) become N_{n-2} and N_n respectively.

$$A_f E_f s_{n-2} - [A_f E_f + \psi k_{n-1} h^2] s_{n-1} = -A_f E_f ss \quad (19)$$

Equilibrium equations of $n-1$ nodes of the embedded length can be expressed by the following expression,

$$[C]_{(n-1),(n-1)} \{S\}_{(n-1)} = \{P\}_{(n-1)} \quad (20)$$

where $[C]$ is a tri-diagonal square matrix, of dimensions $(n-1) \times (n-1)$, collecting coefficients, $\{S\}$ is the vector of the unknown nodal slips, and $\{P\}$ is the vector of the known driving force, determined by prescribed slip ss . In order to run the first step of the iteration, ss must be sufficiently small to ensure that each node remains in the elastic branch of the CML, so that $k_1 = k_{ni} = k_{n-1} = \tau_1/u_1$. In further steps, values of K_i are updated on the basis of the nodal slip obtained by the solution of equation (20) at the previous step. At each step of the iteration, a convergence check, i.e., $\frac{|k^j - k^{j-1}|}{k_{ref}} < tol$, is carried

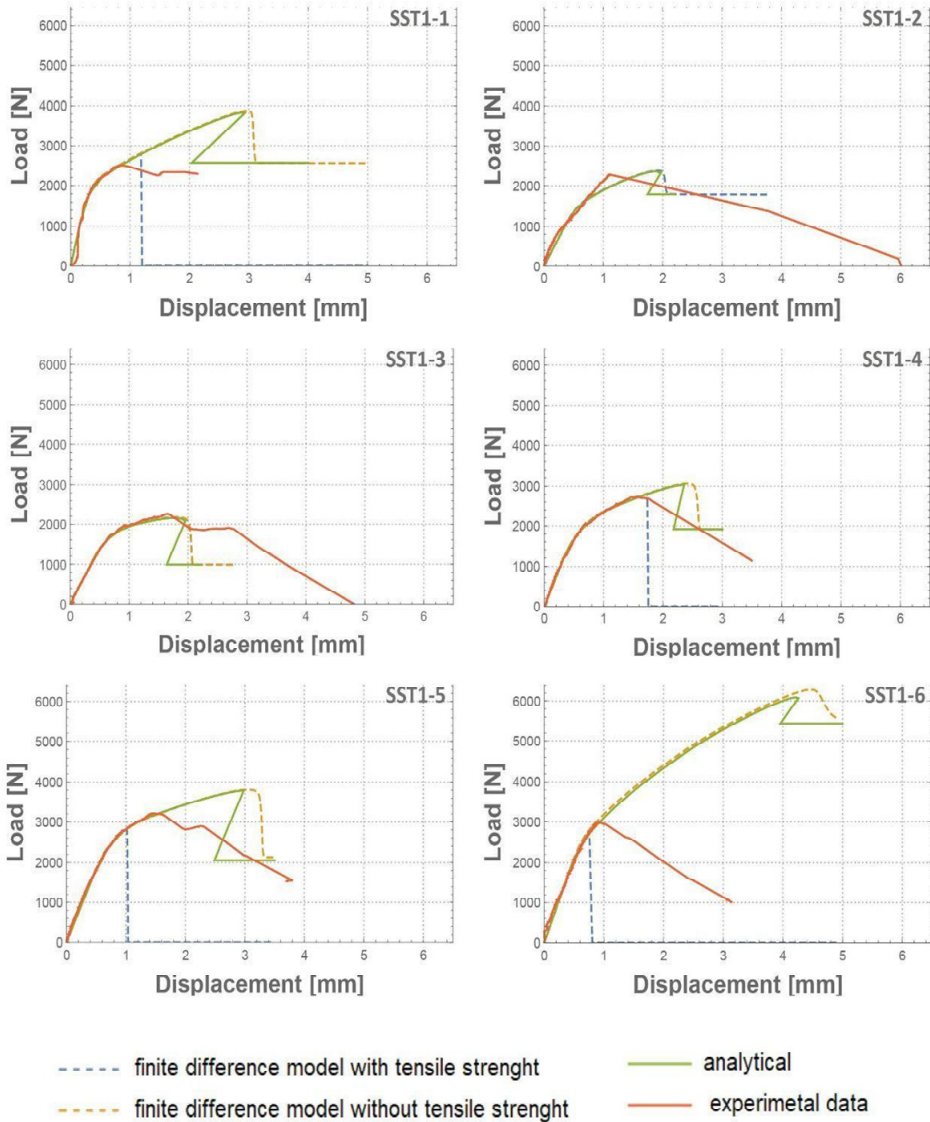
out to ensure that the difference value of the secant modulus at subsequent steps is below the tolerance value. In case the tolerance check is not satisfied, the secant modulus K_i is recalibrated through the correction factor ζk .

3.3 Analytical and numerical model application

The finite-difference model is applied to interpret the experimental data of all the specimens of composite type 1, which showed a failure mode commenced with the slippage of the fibre textile within the matrix and final fibre rupture. The number of elements for the domain discretisation, the increment of displacement at each step of the iteration and the tolerance for the secant modulus k_i between consequent steps are chosen through a parametric study. Embedded lengths are discretised with millimetric spacing, i.e., $h = 1$ mm, and the prescribed displacement at loaded end ss is iteratively incremented of 0.01 mm until reaching the frictional debonding phase. Tolerance is set at 10%.

For specimens SST1-2, SST1-3, SST1-4 and SST1-5, the finite-difference model estimation of the global load-slip curve showed a high degree of accuracy. The premature tensile rupture of fibre in specimens SST1-1 and SST1-6 is satisfactorily tackled as well through the limited tensile capacity of the fibre included in the model.

Figure 12 Specimen type SST1: analytical and numerical model estimation superposed to experimental outcomes (see online version for colours)



Also, although both the analytical and the numerical procedure correctly capture the composite behaviour in terms of global load-slip diagram until peak load, some discrepancies are encountered in the post-peak phase (see Figure 12). After the attainment of maximum load, in the analytical solution a decrease of the slip, i.e., a snap-back, is described, although not observed experimentally; this fact is connected to the solution of the differential equations (Yuan et al., 2004). Conversely, as in the displacement-controlled experimental testing procedure, iterations of the finite difference

model are driven by the known displacement ss , which is prescribed incrementally, thus preventing decrease of the slip value in the global load-slip diagram.

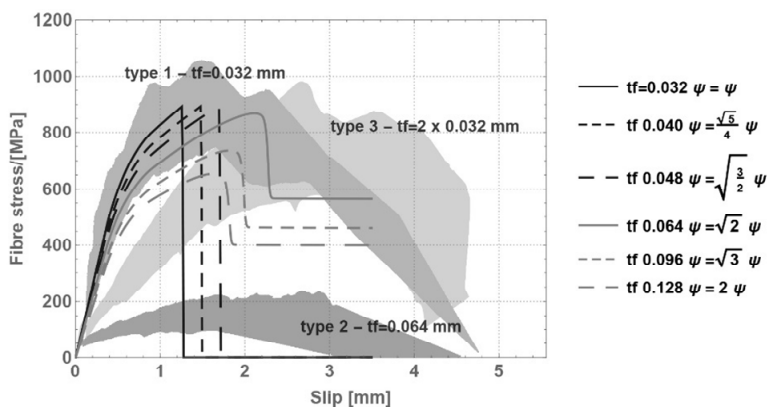
Furthermore, without considering a limited tensile capacity of the fibre, analytical and numerical estimations are higher than experimental data for all specimens in which fibre tensile strength was reached at the end of the test (SST1-1, SST1-4, SST1-5, SST1-6). The possibility of introducing the limited tensile strength of the fibre offers a closer estimation of experimental peak loads (Figure 12).

3.4 Discussion of results

Results of experimental tests highlight that increasing reinforcement ratio by shrinking spacing or doubling layers of textile do not provide the same increase in bearing capacity of the jacket, see Figure 9. Estimating design parameters for the three composite types according to Consiglio Nazionale delle Ricerche (2018), provides a clear insight. The conventional limit strength and limit strain, assuming results of fibre tensile tests for Young’s modulus, show comparable design parameters for the looser mesh with one or two layers, i.e., 875 MPa and 0.0171 for single layer and 825 MPa and 0.016 for two layers. For the tighter mesh, the conventional limit strength and limit strain are, respectively, 169 MPa and 0.003.

Figure 13 shows, superposed to the experimental results as shaded areas, estimation of stress-slip diagrams obtained through the finite difference model based on an average CML for the reinforcement type 1, defined by the following values (δ_1 0.342 mm $-\tau_1$ 1.749 MPa; δ_2 0.892 mm $-\tau_2$ 0.697 MPa). In Figure 13, the increasing reinforcement ratios are sorted with reference to the equivalent thickness. The bonding surface increase corresponding to equivalent thickness increase, is hence indicated as a coefficient of the bonding perimeter ψ , associated with the reference equivalent thickness, i.e., $t_f^* = 0.032$.

Figure 13 Finite difference stress-slip diagrams for varying reinforcement ratios superposed to experimental outcomes, t_f^* is the equivalent thickness and ψ is the perimeter of the fibre



SST1 type shows $t_f^* = 0.032$ mm and the corresponding bonding perimeter has been defined as ψ . SST3 shows, double t_f^* and double bonding surface of SST1. Hence, the

upper continuous stress-slip curve ($t_f^* = 0.032$ mm, $\psi = \psi$) in Figure 13 represents in the finite difference model both SST1 and SST3 since the ratio fibre cross-section vs. bonding perimeter is the same. Nonetheless, in the experimental campaign SST3 sample showed a response more deformable than sample SST1, confirming that two textile layers do not activate efficiently all the available bonding surface.

Moreover, for the SST2 sample, which shows $t_f^* = 0.064$ mm and $\psi = \sqrt{2}\psi$, a marked difference between numerical predictions and experimental results is noticeable. The difference is owed to the failure mode, i.e., fibre-matrix debonding rather than sliding, which depends, in addition to fibre cross section and bonding surface (represented in the model), also on the textile layout that the model cannot tackle.

For the considered CML and fibre tensile strength, equivalent thickness $t_f^* = 0.064$ mm constitutes the threshold value between fibre rupture and sliding failure modes. Also, stress-slip diagrams predicted by the finite difference model show that increasing the reinforcement ratio although increasing the load bearing capacity, clearly induces a decrease in the stress levels reached, consistently with the results of the experimental campaign.

Interestingly, increasing reinforcement amount inhibits the slip capacity of the system, or rather, reduces the outreach of the elastic-softening-friction branch of the diagram. Hence, for a fixed value of the slip, the parts of the reinforcement experiencing the different phases of the CML (elastic, softening, friction) show different lengths. For a certain slip value, the reinforcements with greater amount of fibre show the shear stress peak in a position closer to the free end; hence, the length of reinforcement in the elastic phase is shorter. Also, for higher fibre ratios, the lengths of the jackets in the softening and in the friction stages of the CML are both longer.

4 Concluding remarks

The paper reports an experimental campaign on a basalt-fibre reinforced composite system coupled with a lime-based mortar. Experimental results of single-lap shear tests, carried out on specimens where meshes with different spacings are embedded, show that increasing the reinforcement ratio by means of shrinking the mesh spacing is detrimental for this type of system. Conversely, if the reinforcement ratio is increased to the same amount, embedding two layers of the wider mesh, bond capacity is not deteriorated and higher load capacity is clearly reached. This fact is remarkably relevant for future investigations and highlights that an optimal balance between spacing and reinforcement ratio exists for each specific system.

Within the fracture process zone framework, it was analytically verified that the tested bond behaviour can be modelled employing a tri-linear CML. In addition to analytical modelling, interpretation of test results is carried out by means of a finite difference numerical model. Both analytical and numerical models satisfactorily tackle the trend of the first phases of the tests, up to the peak load, providing close estimations of the experimental results. In the post-peak phase, the finite difference model qualitatively better reproduces results of single direct shear tests. The finite difference

model in fact simulates an imposed displacement test like the experimental one, recording a negative slope softening branch after the peak.

Estimations of analytical models diverge from experimental global load-slip diagrams when the rupture of the fibre, caused by reaching its tensile strength, is registered. The finite difference model, on the other hand, can reproduce the experimental diagram on this aspect as well, being able to control the tensile limit value of the fibre.

The development of an agile numerical model calibrated through experimental tests, as the one proposed in this study can provide a useful analysis tool to:

- 1 evaluate the influence of the key factors (as properties of the materials and cohesive law) on the mechanical behaviour
- 2 optimise the composite system, changing geometric and volumetric ratios of the components
- 3 compare different systems, varying type of components.

The individuation of consistency and divergence among models and between models and experimental results raise awareness on the influence of modelling systems on results estimations. Hence, the study provides a novel groundwork for further implementations.

It is also noteworthy that much lower computational effort is needed in the finite difference model, compared to the analytical one. This aspect is of crucial importance when several parameters are considered for the characterisation of the composite material, which would result in complex systems of differential equations in the analytical solution.

Further investigations will focus on refinement of the model, including mortar deformability and mesh layout.

References

- ACI Committee 549 (2013) *Guide to Design and Construction of Externally Bonded Fabric-Reinforced Cementitious Matrix (FRCM) Systems for Repair and Strengthening Concrete Structures*, ACI Webinar Notes.
- Alecci, V., Misseri, G., Rovero, L., Stipo, G., De Stefano, M., Feo, L. and Luciano, R. (2016) 'Experimental investigation on masonry arches strengthened with PBO-FRCM composite', *Composites Part B: Engineering*, Vol. 100, pp.228–239, doi: 10.1016/j.compositesb.2016.05.063.
- Barducci, S., Alecci, V., De Stefano, M., Misseri, G., Rovero, L. and Stipo, G. (2020) 'Experimental and analytical investigations on bond behavior of Basalt-FRCM systems', *Journal of Composites for Construction, American Society of Civil Engineers (ASCE)*, Vol. 24, No. 1, p.04019055, doi: 10.1061/(asce)cc.1943-5614.0000985.
- Bilotta, A. and Lignola, G.P. (2021) 'Effect of fiber-to-matrix bond on the performance of inorganic matrix composites', *Composite Structures*, Vol. 265, p.113655, doi: 10.1016/j.compstruct.2021.113655.
- Boem, I. and Gattesco, N. (2021) 'Cyclic behavior of masonry barrel vaults strengthened through composite reinforced mortar, considering the role of the connection with the abutments', *Engineering Structures*, Vol. 228, p.111518, Elsevier, doi: 10.1016/J.ENGSTRUCT.2020.111518.

- Briccoli Bati, S., Rovero, L. and Tonietti, U. (2007) 'Strengthening masonry arches with composite materials', *Journal of Composites for Construction, American Society of Civil Engineers (ASCE)*, Vol. 11, No. 1, pp.33–41, doi: 10.1061/(asce)1090-0268(2007)11:1(33).
- Caggegi, C., Lanoye, E., Djama, K., Bassil, A. and Gabor, A. (2017) 'Tensile behaviour of a basalt TRM strengthening system: Influence of mortar and reinforcing textile ratios', *Composites Part B: Engineering*, Vol. 130, pp.90–102, Elsevier Ltd, doi: 10.1016/j.compositesb.2017.07.027.
- Carozzi, F.G., Milani, G. and Poggi, C. (2014) 'Mechanical properties and numerical modeling of Fabric Reinforced Cementitious Matrix (FRCM) systems for strengthening of masonry structures', *Composite Structures*, Vol. 107, pp.711–725, Elsevier, doi: 10.1016/J.COMPSTRUCT.2013.08.026.
- Ceroni, F. and Salzano, P. (2018) 'Design provisions for FRCM systems bonded to concrete and masonry elements', *Composites Part B: Engineering*, Vol. 143, pp.230–242, Elsevier Ltd, doi: 10.1016/j.compositesb.2018.01.033.
- Consiglio Nazionale delle Ricerche (2018) 'CNR-DT 215/2018 Istruzioni per la Progettazione, l'Esecuzione ed il Controllo di Interventi di Consolidamento Statico mediante l'utilizzo di Compositi Fibrorinforzati a Matrice Inorganica', CNR: Consiglio Nazionale delle Ricerche.
- Dalalbashi, A., Ghiassi, B., Oliveira, D.V. and Freitas, A. (2018a) 'Effect of test setup on the fiber-to-mortar pull-out response in TRM composites: experimental and analytical modeling', *Composites Part B: Engineering*, Vol. 143, pp.250–268, Elsevier Ltd, doi: 10.1016/j.compositesb.2018.02.010.
- Dalalbashi, A., Ghiassi, B., Oliveira, D.V. and Freitas, A. (2018b) 'Fiber-to-mortar bond behavior in TRM composites: Effect of embedded length and fiber configuration', *Composites Part B: Engineering*, Vol. 152, pp.43–57, Elsevier Ltd, doi: 10.1016/j.compositesb.2018.06.014.
- De Santis, S., Hadad, H.A., Asce, S.M., De Caso, Y., Basalo, F., Asce, A.M., De Felice, G., Nanni, A. and Asce, F. (2018) *Acceptance Criteria for Tensile Characterization of Fabric-Reinforced Cementitious Matrix Systems for Concrete and Masonry Repair*, doi: 10.1061/(ASCE)CC.1943.
- Donnini, J., Lancioni, G. and Corinaldesi, V. (2018) 'Failure modes in FRCM systems with dry and pre-impregnated carbon yarns: Experiments and modeling', *Composites Part B: Engineering*, Vol. 140, pp.57–67, Elsevier, doi: 10.1016/J.COMPOSITESB.2017.12.024.
- EN-1015-11 (2019) 'Methods of test for mortar for masonry – Part: 11 determination of flexural and compressive strength of hardened mortar', *European Norm*, Vol. 11, pp.1–15.
- Fazzi, E., Misseri, G., Rovero, L. and Stipo, G. (2022) 'Finite difference model for the bond behaviour of polyparaphenylene benzobisoxazole (PBO) Fibre-Reinforced Composite System for Retrofitting Masonry', in *Mechanics of Masonry Structures Strengthened with Composite Materials IV*, Trans Tech Publications Ltd (Key Engineering Materials), pp.425–432.
- Gattesco, N. and Boem, I. (2019) 'Review of experimental tests and numerical study on masonry vaults reinforced through fiber-reinforced mortar coating', *Bulletin of Earthquake Engineering*, Vol. 17, No. 7, pp.4027–4048, Springer Netherlands, doi: 10.1007/s10518-019-00619-y.
- Grande, E. and Milani, G. (2018) 'Interface modeling approach for the study of the bond behavior of FRCM strengthening systems', *Composites Part B: Engineering*, Vol. 141, pp.221–233, Elsevier, doi: 10.1016/j.compositesb.2017.12.052.
- Grande, E., Imbimbo, M. and Sacco, E. (2018) 'Numerical investigation on the bond behavior of FRCM strengthening systems', *Composites Part B: Engineering*, Vol. 145, pp.240–251, Elsevier, doi: 10.1016/J.COMPOSITESB.2018.03.010.
- Kouris, L.A.S. and Triantafillou, T.C. (2018) 'State-of-the-art on strengthening of masonry structures with textile reinforced mortar (TRM)', *Construction and Building Materials*, pp.1221–1233, Elsevier Ltd, doi: 10.1016/j.conbuildmat.2018.08.039.

- Kumar, P., Rao Padalu, V., Singh, Y. and Das, S. (2019) 'Out-of-plane flexural strengthening of URM wallties using basalt fibre reinforced polymer composite', *Construction and Building Materials*, Vol. 216, pp.272–295, doi: 10.1016/j.conbuildmat.2019.04.268.
- Lignola, G.P., Caggegi, C., Ceroni, F., De Santis, S., Krajewski, P., Lourenço, P.B., Morganti, M., Papanicolaou, C. (Corina), Pellegrino, C., Prota, A. and Zuccarino, L. (2017) 'Performance assessment of basalt FRCM for retrofit applications on masonry', *Composites Part B: Engineering*, Vol. 128, pp.1–18, Elsevier Ltd, doi: 10.1016/j.compositesb.2017.05.003.
- Misseri, G., Rovero, L. and Galassi, S. (2021) 'Analytical modelling bond behaviour of polybenzoxazole (PBO) and glass fibre reinforced cementitious matrix (FRCM) systems coupled with cement and gypsum matrices: effect of the cohesive material law (CML) shape', *Composites Part B: Engineering*, Vol. 223, p.109090, Elsevier, doi: 10.1016/J.COMPOSITESB.2021.109090.
- Misseri, G., Rovero, L., Stipo, G., Barducci, S., Alecci, V. and De Stefano, M. (2019a) 'Experimental and analytical investigations on sustainable and innovative strengthening systems for masonry arches', *Composite Structures*, Vol. 210, doi: 10.1016/j.compstruct.2018.11.054.
- Misseri, G., Stipo, G., Galassi, S. and Rovero, L. (2019b) 'Experimental investigation on the bond behaviour of basalt trm systems-influence of textile configuration and multi-layer application', *Key Engineering Materials*, doi: 10.4028/www.scientific.net/KEM.817.134.
- Misseri, G., Stipo, G., Galassi, S. and Rovero, L. (2020) 'Bond behavior of TRM systems and reinforcement of masonry arches: testing and modelling', in Carcaterra, A., Paolone, A. and Graziani, G. (Eds.): *Proceedings of XXIV AIMETA Conference 2019*, Springer International Publishing, Cham, pp.558–570.
- Monaldo, E., Nerilli, F. and Vairo, G. (2019) 'Basalt-based fiber-reinforced materials and structural applications in civil engineering', *Composite Structures*, Vol. 214, pp.246–263, Elsevier, doi: 10.1016/J.COMPSTRUCT.2019.02.002.
- Nerilli, F., Marfia, S. and Sacco, E. (2020) 'Micromechanical modeling of the constitutive response of FRCM composites', *Construction and Building Materials*, Vol. 236, p.117539, Elsevier Ltd, doi: 10.1016/j.conbuildmat.2019.117539.
- Padalu, P.K.V.R., Singh, Y. and Das, S. (2020) 'Analytical modelling of out-of-plane flexural response of unreinforced and strengthened masonry walls', *Engineering Structures*, Vol. 218, p.110797, Elsevier, doi: 10.1016/J.ENGSTRUCT.2020.110797.
- Razavizadeh, A., Ghiassi, B. and Oliveira, D.V. (2014) 'Bond behavior of SRG-strengthened masonry units: testing and numerical modeling', *Construction and Building Materials*, Vol. 64, pp.387–397, Elsevier, doi: 10.1016/J.CONBUILDMAT.2014.04.070.
- RILEM TC 250-CSM (2018) 'Recommendation of RILEM Technical Committee 250-CSM: test method for textile reinforced mortar to substrate bond characterization', *Materials and Structures/Materiaux et Constructions*, Vol. 51, No. 4, pp.1–9, Springer, Netherlands, doi: 10.1617/s11527-018-1216-x.
- Rotunno, T., Rovero, L., Toniatti, U. and Bati, S.B. (2015) 'Experimental study of bond behavior of CFRP-to-Brick joints', *Journal of Composites for Construction, American Society of Civil Engineers (ASCE)*, Vol. 19, No. 3, p.04014063, doi: 10.1061/(asce)cc.1943-5614.0000528.
- Rovero, L., Focacci, F. and Stipo, G. (2013) 'Structural behavior of arch models strengthened using fiber-reinforced polymer strips of different lengths', *Journal of Composites for Construction, American Society of Civil Engineers (ASCE)*, Vol. 17, No. 2, pp.249–258, doi: 10.1061/(asce)cc.1943-5614.0000325.
- Rovero, L., Galassi, S. and Misseri, G. (2020) 'Experimental and analytical investigation of bond behavior in glass fiber-reinforced composites based on gypsum and cement matrices', *Composites Part B: Engineering*, Vol. 194, p.108051, doi: 10.1016/j.compositesb.2020.108051.

- Soranakom, C. and Mobasher, B. (2010a) 'Modeling of tension stiffening in reinforced cement composites: Part I. Theoretical modeling', *Materials and Structures*, Vol. 43, No. 9, Springer, pp.1217–1230, doi: 10.1617/S11527-010-9594-8.
- Soranakom, C. and Mobasher, B. (2010b) 'Modeling of tension stiffening in reinforced cement composites: Part II. Simulations versus experimental results', *Materials and Structures/Materiaux et Constructions*, Vol. 43, No. 9, pp.1231–1243, Springer, doi: 10.1617/s11527-010-9593-9.
- Yuan, H., Teng, J.G., Seracino, R., Wu, Z.S. and Yao, J. (2004) 'Full-range behavior of FRP-to-concrete bonded joints', *Engineering Structures*, Vol. 26, pp.553–565, doi: 10.1016/j.engstruct.2003.11.006.